Active and Passive Tuning of Ultranarrow Resonances in Polaritonic Nanoantennas

Jiahua Duan,* Francisco Javier Alfaro-Mozaz, Javier Taboada-Gutiérrez, Irene Dolado, Gonzalo Álvarez-Pérez, Elena Titova, Andrei Bylinkin, Ana Isabel F. Tresguerres-Mata, Javier Martín-Sánchez, Song Liu, James H. Edgar, Denis A. Bandurin, Pablo Jarillo-Herrero, Rainer Hillenbrand, Alexey Y. Nikitin,* and Pablo Alonso-González*

Optical nanoantennas are of great importance for photonic devices and spectroscopy due to their capability of squeezing light at the nanoscale and enhancing light–matter interactions. Among them, nanoantennas made of polar crystals supporting phonon polaritons (phononic nanoantennas) exhibit the highest quality factors. This is due to the low optical losses inherent in these materials, which, however, hinder the spectral tuning of the nanoantennas due to their dielectric nature. Here, active and passive tuning of ultranarrow resonances in phononic nanoantennas is realized over a wide spectral range (≈35 cm^{-1}, being the resonance linewidth ≈9 cm^{-1}), monitored by near-field nanoscopy. To do that, the local environment of a single nanoantenna made of hexagonal boron nitride is modified by placing it on different polar substrates, such as quartz and 4H-silicon carbide, or covering it with layers of a high-refractive-index van der Waals crystal (WSe$_2$). Importantly, active tuning of the nanoantenna polaritonic resonances is demonstrated by placing it on top of a gated graphene monolayer in which the Fermi energy is varied. This work presents the realization of tunable polaritonic nanoantennas with ultranarrow resonances, which can find applications in active nanooptics and (bio)sensing.

1. Introduction

Polaritons,[1–3] light coupled to coherently oscillating charges, enable strong enhancement and confinement of electromagnetic fields at dimensions deep below the incident wavelength. They are thus attractive for numerous applications, such as nanoscale light trapping,[4] single molecule sensing,[5–7] or photodetection.[8] Typically, plasmon polaritons—collective oscillations of free electrons coupled to photons—at metal or semiconductor surfaces have been employed to design plasmonic antennas for light manipulation[9,10] and enhanced spectroscopy.[11–13] However, the problems of large absorption losses[14,15] and lack of active tunability impose severe limitations to manipulate plasmon polaritons in metals. As a promising alternative, the semimetal graphene

J. Duan, J. Taboada-Gutiérrez, G. Álvarez-Pérez, A. I. F. Tresguerres-Mata, J. Martín-Sánchez, P. Alonso-González
Department of Physics
University of Oviedo
Oviedo 33006, Spain
E-mail: duanjiahua@uniovi.es; pabloalonso@uniovi.es

J. Duan, J. Taboada-Gutiérrez, G. Álvarez-Pérez, A. I. F. Tresguerres-Mata, J. Martín-Sánchez, P. Alonso-González
Center of Research on Nanomaterials and Nanotechnology
CINN (CSIC–Universidad de Oviedo)
El Entrego 33940, Spain

F. J. Alfaro-Mozaz, I. Dolado, A. Bylinkin
CIC nanoGUNE
BRTA
Donostia-San Sebastian 20018, Spain

E. Titova
Programmable Functional Materials Lab
Brain and Consciousness Research Center
Moscow 121205, Russia

E. Titova
Center for Photonics and 2D Materials
Moscow Institute of Physics and Technology
Dolgoprudny 141701, Russia

A. Bylinkin, A. Y. Nikitin
Donostia International Physics Center (DIPC)
Donostia-San Sebastian 20018, Spain
E-mail: alexey@dipc.org

S. Liu, J. H. Edgar
Tim Taylor Department of Chemical Engineering
Kansas State University
Manhattan, KS 66506, USA

D. A. Bandurin, P. Jarillo-Herrero
Department of Physics
Massachusetts Institute of Technology (MIT)
Boston, MA 02139, USA

R. Hillenbrand, A. Y. Nikitin
IKERBASQUE
Basque Foundation for Science
Bilbao 48013, Spain

ADVANCED
SCIENCE NEWS
www.advancedsciencenews.com

ADVANCED
MATERIALS
www.advmat.de

has recently opened new opportunities for the development of active subwavelength-scale optics[16,17] and robust plasmonic biosensors[18] due to its tunable plasmonic response[19,20] and high degree of light confinement.[21–23] On the other hand, phonon polaritons (PhPs)[24]—hybrid waves resulting from the coupling of crystal lattice vibrations and photons—have been far less studied compared to their plasmonic counterparts. However, PhPs-based phononic nanoantennas provide significantly improved field enhancements and quality factors[25–28] compared to plasmonic nanoantennas due to the suppression of Ohmic losses. Some van der Waals (vdW) materials[29–31] exhibit mid-infrared PhPs with a record-high lifetime (up to 20 ps) in the so-called reststrahlen bands, defined as the frequency region between the transverse optical and longitudinal optical phonons and in which the dielectric permittivity is negative, hence enabling the existence of polaritonic modes. For instance, hexagonal boron nitride (h-BN) is a uniaxial hyperbolic vdW material,[32] whose real-part of the parallel ($\varepsilon_{\parallel}$) and perpendicular ($\varepsilon_{\perp}$) dielectric permittivities have opposite signs. This optical property of h-BN enables the propagation of low-loss PhPs featuring hyperbolic dispersion and large density of optical states, which is important for strong field confinement[33,34] and enhancement of light–matter interactions.[25] Large-quality-factor (Q) PhP resonances in h-BN cone-shaped and linear (dipolar) nanoantennas have been demonstrated by recent nanospectroscopy experiments,[25,28,35] revealing the broad application prospects of phononic nanoantennas made of hyperbolic materials in infrared (IR) nanophotonics (e.g., for refractive index sensing[28] or surface-enhanced infrared absorption spectroscopy[36,37]). However, since the properties of PhPs are dictated by the crystal lattice dynamics, spectral tuning of PhPs is challenging. Although control of the dispersion of propagating PhPs was achieved by combining h-BN slabs with gated graphene,[38,39] spectral tuning of the resonances in phononic nanoantennas remains elusive, yet it is very appealing due to their large Q.

Here, we demonstrate active and passive tuning of ultranarrow resonances in phononic nanoantennas, namely h-BN squares with a nanoscale cross-section. Our nanoimaging experiments and numerical simulations reveal sharp resonances with linewidths of around 9 cm^{-1} ($Q \approx 165$), which generate puzzling near-field patterns that allow shrinking mid-infrared light (of incident wavelength λ_0) to subwavelength dimensions ($\approx \lambda_0/42$). Passive tuning of these ultranarrow resonances is demonstrated over several resonance linewidths by modifying the dielectric environment of the phononic nanoantenna. This modification is realized by placing the nanoantenna on different substrates as well as covering it with different superstrates (without moving the nanoantenna). Importantly, we also demonstrate the realization of actively tunable nanoantennas with ultranarrow resonances (linewidths of ≈ 20 cm^{-1}, i.e., one order of magnitude smaller than the typical linewidths in active graphene nanoantennas) by placing them on top of

R. Hillenbrand
CIC nanoGUNE
BRTA and Department of Electricity and Electronics
EHU/UPV
Donostia-San Sebastián 20018, Spain

gated graphene in which we vary the Fermi energy. Our results establish the basis for the control of polaritonic resonances in nanoantennas made of hyperbolic materials, while the combination of refractive-index sensitivity and active tunability of ultranarrow resonances opens exciting prospects for biosensing and the realization of tunable strong coupling phenomena at the nanoscale.

2. Infrared Nanoimaging of Square h-BN Nanoantennas

To study the polaritonic resonances in phononic nanoantennas made of vdW hyperbolic materials, we fabricate h-BN squares with a nanoscale cross-section and carry out near-field measurements by employing scattering-type scanning near-field optical microscopy (s-SNOM). To nanoimage the square h-BN nanoantennas, we illuminate the s-SNOM tip with p-polarized monochromatic mid-IR light and record the amplitude of the tip-scattered field as a function of the tip position (see schematics in **Figure 1**a). PhPs propagate radially outward from the tip, reflect upon reaching the corners and edges of the nanoantennas, and modify the tip-scattered light when they return to the tip. By raster scanning the nanoantenna surface at different incident frequencies (ω_0), we observe complex near-field modal patterns with bright dots at the edges and a variety of features inside the nanoantenna (Figure 1b–i). Interestingly, the near-field patterns change dramatically even with a slight variation of ω_0. For instance, one single bright spot appearing in the center of the nanoantenna at $\omega_0 = 1490$ cm^{-1} (Figure 1e) changes to a dark spot surrounded by a bright ring for a frequency shift of only 10 cm^{-1} at $\omega_0 = 1500$ cm^{-1} (Figure 1f). To study the origin of these near-field patterns, we extract the PhP wavevector q by taking a line profile in the experimental near-field amplitude images, both inside the nanoantennas (lower panels in Figure 1b–i) and at their periphery (see the Supporting Information). We determine q by using the relation $q = \pi/L$, where L is the distance between the adjacent maxima in the amplitude line profile.[26] When ω_0 increases from $\omega_0 = 1450$ cm^{-1} (Figure 1b) to $\omega_0 = 1540$ cm^{-1} (Figure 1i), the number of peaks (lower panels in Figure 1b–i) gradually increases from one (Figure 1b) to seven (Figure 1i). Such a dramatic increase of the number of peaks is an important implication of a spectrally evolving standing wave pattern, clearly indicating a set of Fabry–Pérot resonances, analogous to those emerging in h-BN linear antennas.[26] In Figure 1j, we show the dispersion ω_0 (q) obtained from experiments (filled symbols) and electromagnetic simulations (solid lines) of the PhP modes in an infinite h-BN slab. Here, M0 (black solid line) and SM0 (red solid line) represent the fundamental volume PhP mode in semi-infinite h-BN slabs[40,41] and fundamental surface-confined PhP mode at the edges of h-BN slabs,[42] respectively. We find a very good agreement between the dispersion curve of the M0 and SM0 modes and the measured data points inside and at the periphery of the nanoantennas, respectively. Thus, we conclude that the combination of fundamental volume and surface-confined PhP modes is the cause of the Fabry–Pérot resonances in the square h-BN nanoantennas.
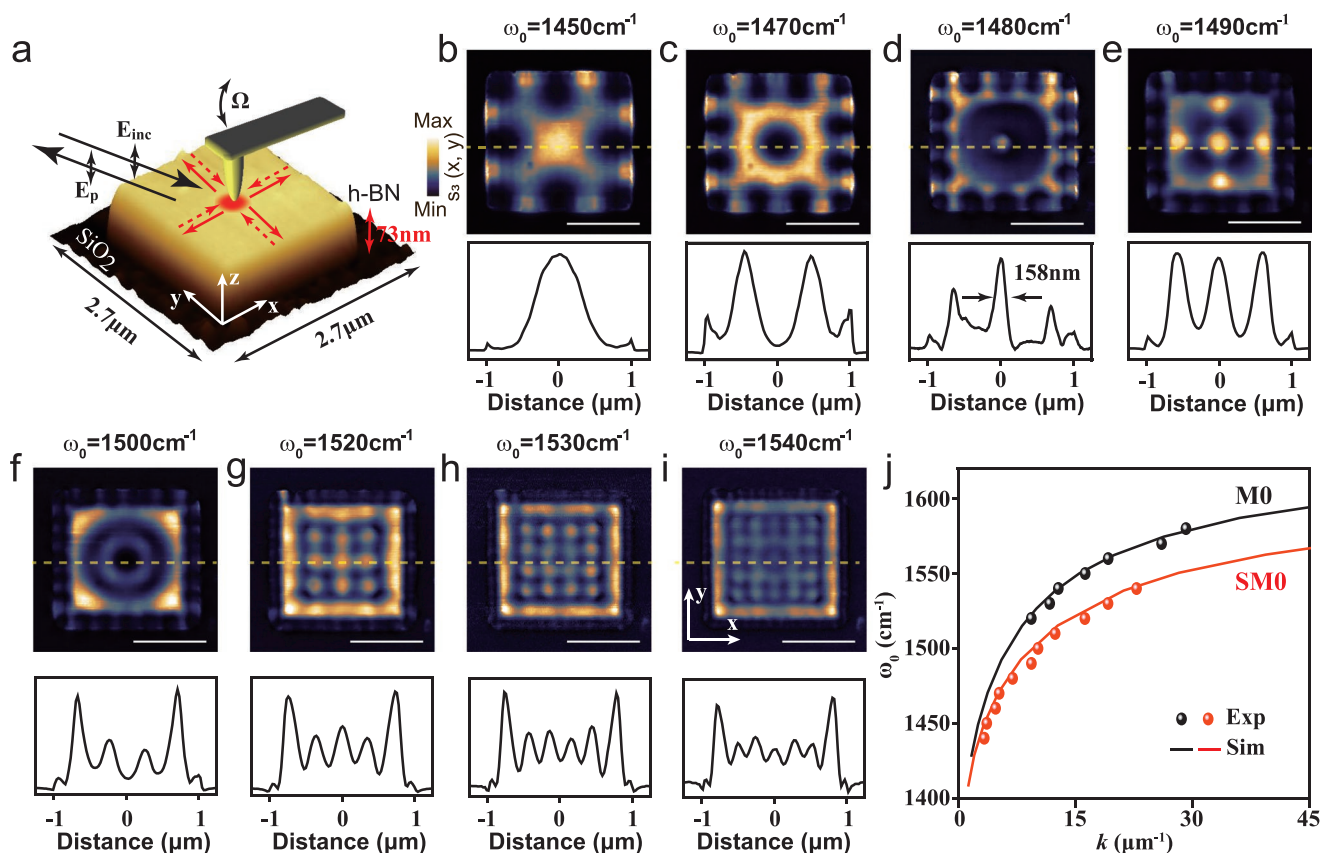
Figure 1. Real-space imaging of polaritonic modes in a square h-BN nanoantenna. a) Schematics of the s-SNOM measurements of a square h-BN nanoantenna. b–i) Upper panels: near-field images of the nanoantenna for incident frequencies (ω_0) of 1450, 1470, 1480, 1490, 1500, 1520, 1530, and 1540 cm^{-1}, respectively. Bottom panels: amplitude line profiles extracted along the dashed lines in the near-field images. Scale bar: 1 μm. j) Simulated (solid lines) dispersions of the fundamental volume-confined (M0) and surface-confined (SM0) hyperbolic modes in a slab of h-BN. The solid symbols represent the experimental results extracted from line profiles inside the nanoantenna (dashed line in (b–i)) and its periphery (Figure S3, Supporting Information), respectively.

As expected for PhPs in h-BN in the reststrahlen band (1395 cm^{-1} ≤ ω_0 ≤ 1630 cm^{-1}),[43] the wavevector q increases with ω_0 for both the M0 and SM0 modes, the latter showing a larger q (i.e., smaller wavelength). When ω_0 is larger than 1500 cm^{-1} (Figure 1g–i), the M0-PhP wavelength is much smaller than the side length (2 μm in this work) of the square h-BN nanoantenna and thus the latter exhibits a typical near-field pattern with periodic bright spots analogous to the case of large ("semi-infinite") h-BN slabs[40] and h-BN linear antennas.[26] However, for smaller ω_0, ranging from 1450 cm^{-1} (Figure 1b) to 1500 cm^{-1} (Figure 1f), the M0-PhP wavelength becomes comparable with the side length of the square nanoantenna, introducing convoluted Fabry–Pérot interferences featuring atypical near-field patterns. Therefore, the near-field patterns inside the square h-BN nanoantennas can be classified into two categories: atypical modal patterns (Figure 1b–f) at relatively small ω_0, and typical periodic patterns (Figure 1g–i) at large ω_0. On the other hand, the much smaller wavelength of the SM0 mode (always smaller than the side length) gives rise to periodic bright spots along the edges of the nanoantennas over the entire frequency range (Figure 1b–i). Note that those atypical modal patterns (Figure 1b–f) originating from Fabry–Pérot resonances have remained elusive until now, since all previous works focused

on the periodic patterns (e.g., fringes or periodic dots)[40,43–45] in the condition that the polariton wavelength is much smaller than the size of h-BN structures. However, some of those atypical patterns provide a nanoscale "hot spot" of deeply subwavelength dimensions (≈$\lambda_0/42$) with respect to the incident mid-IR light (λ_0 = 6.76 μm). Such "hot spot" largely shrinks the huge gap between the IR light wavelength (of micrometer size) and the size of molecules (sub-nanometer size), and thus could enhance light–molecule interactions and find applications in molecular spectroscopy.

3. Modal Analysis of Fabry–Pérot Resonances in Square h-BN Nanoantennas

We further elaborate on the formation of near-field patterns in our square h-BN nanoantennas (Figure 1) by performing full-wave numerical simulations (see details in the Experimental Section). To do that, we approximate the s-SNOM tip by a vertical electric dipole source[46] which launches PhPs in the nanoantennas. For each in-plane location of the dipole, we plot the amplitude of the simulated out-of-plane component of the electric near-field ($|E_z|$) below the dipole as a function of frequency,
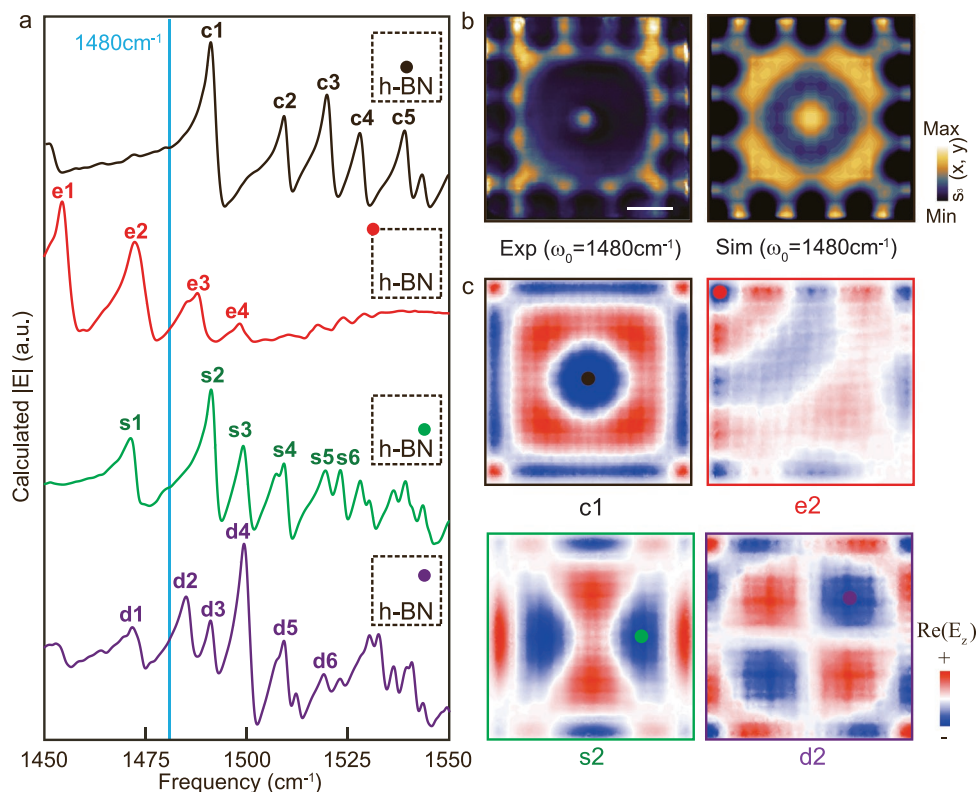
**ADVANCED
SCIENCE NEWS**

www.advancedsciencenews.com

**ADVANCED
MATERIALS**

www.advmat.de

Figure 2. Analysis of the polaritonic modes excited in a square h-BN nanoantenna. a) Simulated near-field spectra obtained by placing a point-dipole source at the nanoantenna center (black), corner (red), flank (green), and diagonal (purple), as indicated by the schematics (dashed square) in each case. The cyan and orange vertical lines represent the incident frequencies $\omega_0 = 1480$ and 1500 cm^{-1}, respectively. b) Experimental (left) and calculated (right) complex near-field patterns in a square h-BN nanoantenna at $\omega_0 = 1480$ cm^{-1}. c) The field distributions for the calculated individual modes at the frequencies of the corresponding peaks: c1 (top left), e2 (top right), s2 (bottom left), and d2 (bottom right) in correspondence with (a). Scale bar: 500 nm.

as shown in **Figure 2**a. Such near-field spectra show a set of closely spaced peaks in a narrow spectral range, associated with the excitation of resonant Fabry–Pérot modes. Different spectral positions of the peaks on different curves indicate that the excitation of PhP modes in the nanoantennas is strongly dependent on the dipole position. For instance, when the dipole is located at the center of the nanoantenna, the spectrum (black solid line in Figure 2a) shows five strong peaks (labeled as c1–c5), which correspond to five individual PhP modes. By contrast, when we locate the dipole at the corner of the nanoantenna, the spectrum (red solid line in Figure 2a) shows four discernable peaks (labeled as e1–e4). On the other hand, when the dipole is located at the flank of the nanoantenna (green solid line in Figure 2a) or its diagonal (purple solid line in Figure 2a), more peaks (labeled as s1–s6 or d1–d6) appear in the spectrum. To connect these near-field spectra with the experimental near-field images, we further simulate the $|E_z|$ as a function of the dipole position by raster scanning the dipole above a square h-BN nanoantenna for two different frequencies. At $\omega_0 = 1480$ cm^{-1}, the experimental near-field image (Figure 2b, left panel) of the nanoantenna shows three clear features, all of which are well reproduced by the simulation (Figure 2b, right panel): i) a bright spot in the center; ii) a bright ring, and iii) four bright spots decorating the edges. We explain this complex pattern in the near-field images by the interference of individual modes,

simultaneously excited due to their spectral overlap for different dipole locations (simulated spectra in Figure 2a). To disentangle the individual modes from this interference pattern, we calculate the spatial near-field distribution above the nanoantenna at the resonant frequencies around $\omega_0 = 1480$ cm^{-1} (cyan line in Figure 2a), as shown in Figure 2c. When the dipole is located at the center of the nanoantenna, we observe a "breathing" mode (c1 mode, top left in Figure 2c), which explains the bright spot and bright ring obtained in the experimental near-field image at $\omega_0 = 1480$ cm^{-1} (Figure 2b, left panel). When the dipole is located at the corner of the nanoantenna, a completely different mode appears (e2 mode, top right in Figure 2c) with field oscillations strongly confined to the edge, revealing the excitation of hyperbolic surface PhPs whose interference with the dipole field produces bright and dark dots along the edges of the nanoantenna as the result of a Fano-like resonance.[46] When the dipole is located at the flank of the nanoantenna (Figure 2c, bottom left) or at its diagonal (Figure 2c, bottom right), we can distinguish the modes s2 and d2 in the field pattern exhibiting a funnel-like shape or four lobes, respectively. Thus, by locating the dipole at these representative positions above the h-BN square nanoantenna, we show that the combination of four individual modes (c1, e2, s2, d2) can explain the experimental near-field image taken at $\omega_0 = 1480$ cm^{-1} (Figure 2b). The interference of these narrow Fabry–Pérot resonances explains the

complex near-field patterns obtained in our square h-BN nano-antennas, which yield "hot spots" with deeply subwavelength volumes as small as ≈150 × 150 × 100 nm³ (Figure 2b).

4. Passive Tuning of the Polaritonic Resonances in a Square h-BN Nanoantenna by Tailoring Its Dielectric Environment

Since polaritons extend as evanescent waves into the media above and below polaritonic nanoantennas, their wavelength is sensitive to the dielectric properties of both the substrate and superstrate. Passive tuning of dispersion of propagating PhPs has been reported with substrate[41,47] and superstrate engineering,[48] yet such tuning of narrow resonances in an individual phononic nanoantenna has never been realized, in spite of its important roles as building blocks in optical circuitry. To do that, we transfer one and the same

square h-BN nanoantenna (see details in the Experimental Section) on two common substrates: silica (SiO_2) and silicon carbide (4H-SiC). At $\omega_0 = 1480$ cm⁻¹, the complex values of the permittivity for SiO_2 and SiC are $\varepsilon_{SiO_2} = 2.01 + 0.01i$ and $\varepsilon_{SiC} = 5.50 + 0.005i$, respectively. Within the regime of a small loss tangent ($Im(\varepsilon)/Re(\varepsilon) < 0.1$),[47] we can neglect the influence on the nanoantenna response of the optical losses of these substrates. The near-field images taken at $\omega_0 = 1480$ cm⁻¹ for the nanoantenna placed on SiO_2 and SiC present significant differences (**Figure 3**). Indeed, a prominent bright spot (Figure 3a) in the center of the nanoantenna on SiO_2 strongly contrasts with a dark spot surrounded by a bright circle (Figure 3b) of the nanoantenna on SiC. Likewise, the number of bright spots along the edges increases from four (Figure 3a) for the SiO_2 substrate to five (Figure 3b) for SiC, clearly indicating that hyperbolic surface polaritons are also very sensitive to the permittivity of the substrate. In contrast to previous spectroscopic measurements in phononic nanoantennas,[28] these images reveal varying PhP modes as a result of the different dielectric
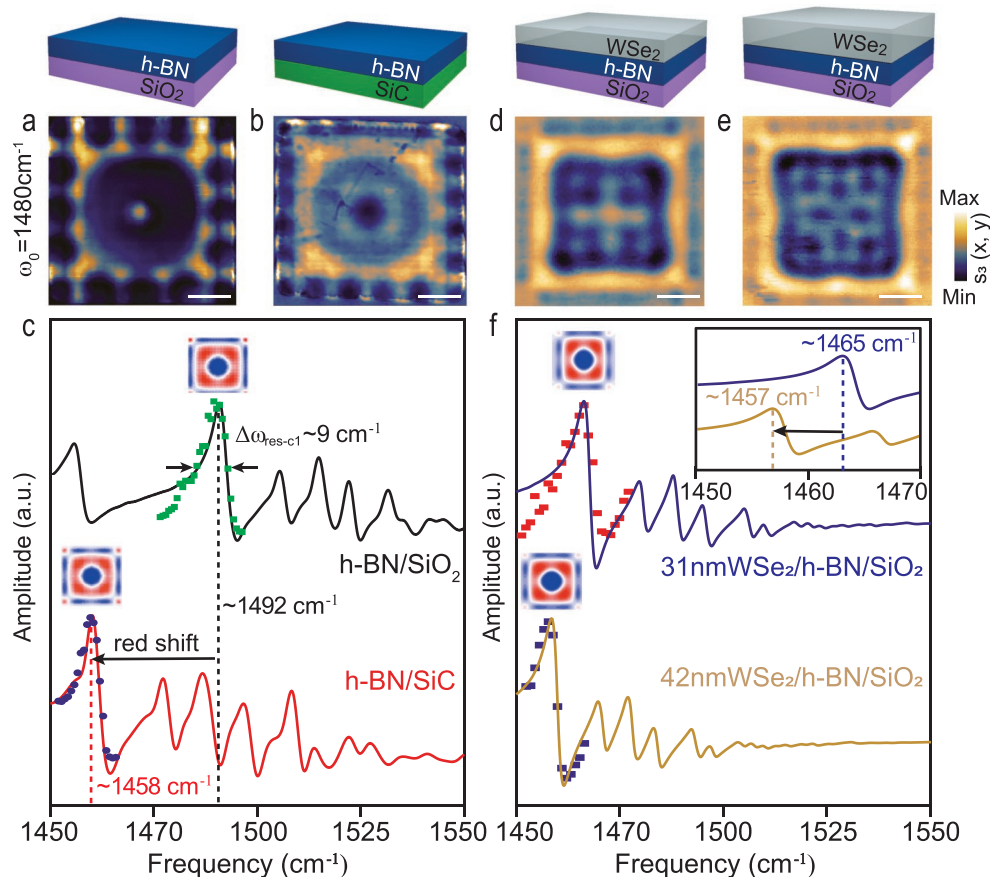

Figure 3. Passive tuning of the polaritonic resonances in a square h-BN nanoantenna by tailoring its dielectric environment. a,b) Near-field images of a square h-BN nanoantenna taken at $\omega_0 = 1480$ cm⁻¹ when it is placed on SiO_2 (a) and SiC (b). c) Calculated near-field spectra for the cases shown in (a) (black solid line) and in (b) (red solid line), respectively. The green and blue dots represent the experimental results in each case. The insets show the calculated field distributions at the resonance peaks corresponding to the c1 mode at $\omega_0 = 1492$ and 1458 cm⁻¹ for the nanoantenna placed on SiO_2 and SiC, respectively. d,e) Near-field images of the nanoantenna taken at $\omega_0 = 1480$ cm⁻¹ when it is placed on SiO_2 and covered with a layer of WSe_2 with thickness of 31 nm (d) and 42 nm (e). f) Calculated near-field spectra for the cases shown in (d) (blue solid line) and in (e) (brown solid line). The red and blue dots represent the experimental results in each case. The insets show the calculated field distribution at the resonance peaks corresponding to the c1 mode at $\omega_0 = 1465$ and 1457 cm⁻¹ for the cases shown in (d) and (e). The zoomed near-field spectra spanning 1450–1470 cm⁻¹ in the inset demonstrate a clear redshift for the resonance peak corresponding to the c1 mode. Scale bar: 500 nm.

nature of the substrate, thus demonstrating passive tuning of the nanoantenna resonances. Notice that the near-field image taken at $\omega_0 = 1480$ cm^{-1} of the nanoantenna on SiC (Figure 3b) appears to be similar to that at $\omega_0 = 1500$ cm^{-1} for the nanoantenna on SiO$_2$ (Figure 2c), indicating that at a fixed ω_0, the PhP wavelength in h-BN/SiC is smaller than that in h-BN/SiO$_2$, thus implying a redshift of the resonances in the nanoantenna. To further elaborate on this frequency shift, we perform nanoimaging spectroscopy at the center of the square h-BN nanoantenna by recording the near-field amplitude at fixed illuminating frequencies (see details in the Experimental Section). The green and blue symbols in Figure 3c represent the experimental results for the nanoantenna on SiO$_2$ and SiC, respectively, showing a good quantitative agreement with the simulated spectra (solid lines in Figure 3c). We observe a clear redshift of the resonant peaks when the substrate is changed from SiO$_2$ (black solid line in Figure 3c) to SiC (orange solid line in Figure 3c). Specifically, for the same c1 mode (the field distribution can be found in the insets to Figure 3c), the resonant frequency (ω_{res-c1}) changes from ≈ 1492 to ≈ 1458 cm^{-1}. Such redshift can be explained by the general rule of a higher refractive-index substrate (SiC) to sustain polaritons with smaller wavelength,[47] which agrees well with our near-field images. We further characterize the quality factor, $Q = \omega_{res}/\Delta\omega_{res}$, where ω_{res} and $\Delta\omega_{res}$ represent the resonant frequency and linewidth of our square h-BN nanoantennas. By fitting the experimental results (green solid symbols in Figure 3c) and taking into account the asymmetric Fano-like shape of the resonant peaks, we approximately estimate (Figure S5, Supporting Information) a linewidth of ≈ 9 cm^{-1} for the peak corresponding to the c1 mode, which yields $Q \approx 165$. This value is comparable to those extracted for other types of phononic nanoantennas[26,28,35] and is much higher than those of typical metallic nanoantennas[49] in the mid-IR range. More importantly, such high Q is accompanied by an extreme subwavelength confinement ($\approx \lambda_0/42$), thus providing an excellent playground for experiments on strong light–matter interactions.

Yet, from a practical perspective, it is much more advantageous to realize passive tuning of the nanoantenna resonances by varying the superstrate rather than the substrate, since by doing so, one can control the PhP modes without moving the nanoantenna. To investigate the modulation of the nanoantenna polaritonic response by changing the superstrate, we cover a square h-BN nanoantenna with thin slabs of WSe$_2$, which exhibits a high dielectric index (Re(ε_{WSe_2}) ≈ 14) in the mid-IR spectral range.[50] As shown in Figure 3d, the near-field pattern in the nanoantenna drastically changes after covering it with a 31 nm-thick layer of WSe$_2$ (Figure 3a). The pattern strongly changes as well when we put another 11 nm-thick layer of WSe$_2$ on top (Figure 3e), so that the nanoantenna gets covered by a superstrate layer with a total thickness of 42 nm. The near-field images of the nanoantennas covered with 31 and 42 nm-thick layers of WSe$_2$ at $\omega_0 = 1480$ cm^{-1} are similar to the ones of the bare nanoantenna at $\omega_0 = 1520$ cm^{-1} (Figure 1g) and $\omega_0 = 1530$ cm^{-1} (Figure 1h), respectively. This indicates that at a fixed ω_0, the PhP wavelength in WSe$_2$-covered h-BN is smaller than that in bare h-BN, thus implying a redshift of the resonances in the square h-BN nanoantennas. To further elaborate on this frequency shift, we perform nanoimaging spectroscopy

at the center of the square nanoantenna by recording the near-field amplitude at fixed illuminating frequencies. The red and blue symbols in Figure 3f represent the experimental results for the nanoantenna covered with 31 and 42 nm of WSe$_2$, respectively. A good quantitative agreement with the simulated spectra (solid lines in Figure 3f) is obtained. There is a clear redshift of the resonant peaks when the thickness of the WSe$_2$ layers changes from 31 nm (blue solid line in Figure 3f) to 42 nm (brown solid line in Figure 3f). Since Re(ε_{WSe_2}) is much larger than 1, such redshift is analogous to the shift obtained when transferring the nanoantenna from a low-refractive-index substrate to a high-refractive-index substrate, e.g., from SiO$_2$ to SiC (Figure 3a,b). Specifically, the peak corresponding to the c1 mode (field distribution in the insets in Figure 3f) shifts from $\omega_{res-c1} \approx 1492$ cm^{-1} for h-BN/SiO$_2$, to $\omega_{res-c1} \approx 1465$ cm^{-1} for 31 nm WSe$_2$/h-BN/SiO$_2$, and finally to $\omega_{res-c1} \approx 1457$ cm^{-1} for 42 nm WSe$_2$/h-BN/SiO$_2$. Altogether, our infrared nanospectroscopy and nanoimaging experiments reveal that low-loss resonances in phononic nanoantennas can be widely tuned by as much as 35 cm^{-1}, which is around 4 times the resonance linewidth (≈ 9 cm^{-1}), by varying dynamically the superstrate of the nanoantennas.

5. Active Tuning of a Polaritonic Resonance in a Square h-BN Nanoantenna by Electrostatic Gating

Although we demonstrate passive tuning of the polaritonic resonances in square h-BN nanoantennas in Figure 3, the challenge of active tuning of these resonances severely limits the technological implementation of phononic nanoantennas. One of the possibilities to actively tune the dispersion of propagating PhPs is to place h-BN slabs on top of a monolayer of graphene.[38] However, a dynamically tunable phononic nanoantenna, which can merge the merits of phononics (e.g., ultralow losses) and graphene plasmonics (e.g., dynamically tuning capability), has never been reported. It is expected that the sharp PhP resonances in our nanoantennas can be controlled via electrostatic gating of a graphene layer placed below (see schematics in **Figure 4**a). By applying a back-gate voltage, we tune the carrier density and thus the Fermi level (E_F) in graphene (see details in the Experimental Section) from 0 to 0.25 eV. For the case of charge neutrality ($E_F = 0$), the near-field image (Figure 4b, left panel) of the square nanoantenna taken at $\omega_0 = 1520$ cm^{-1} exhibits a dark spot surrounded by a bright ring in the center, in good agreements with numerical simulations mimicking the experiment (Figure 4c, left panel). Remarkably, when E_F increases to 0.25 eV, the dark spot at the center of the nanoantenna both in the experimental and simulated near-field images transforms into a bright spot (right panels in Figure 4b,c, respectively).

Such a significant change of the near-field image provides a direct evidence of an active tuning of the PhP modes in the square h-BN nanoantenna at a fixed imaging frequency. We also corroborate the tuning of the spectral shift of the resonant modes in the nanoantenna by simulating the near-field spectra generated by a point dipole fixed at its center for different doping levels (Figure 4d). The resonant peaks experience a clear blueshift with increasing E_F, specifically, the resonant
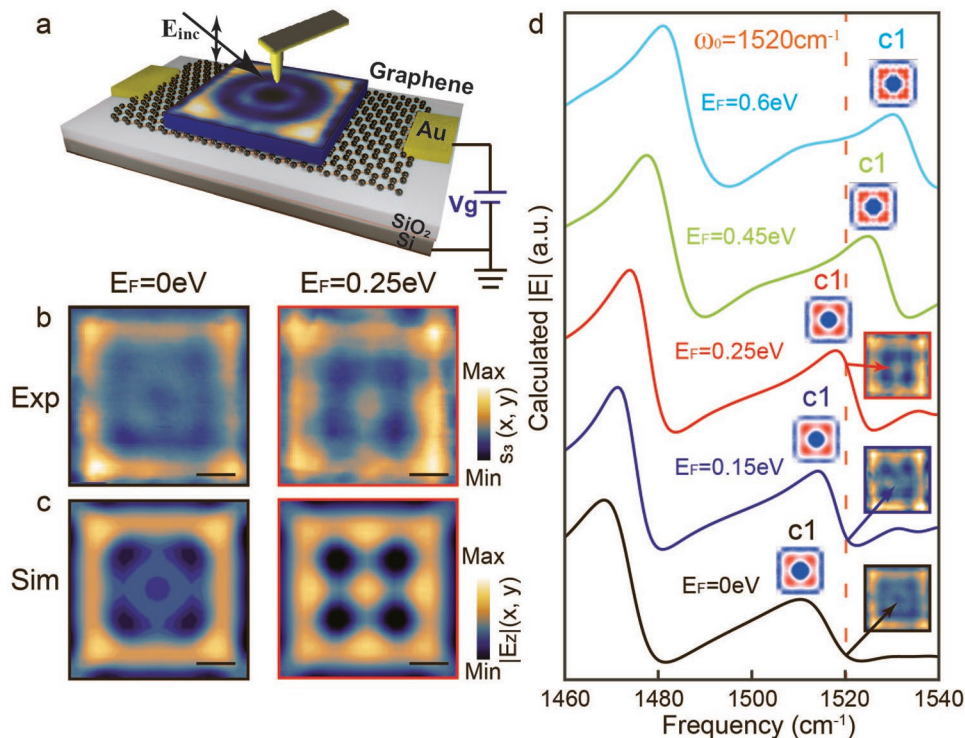
Figure 4. Active tuning of a polaritonic resonance in a square h-BN nanoantenna by electrostatic gating. a) Schematics of the s-SNOM measurements of a square h-BN nanoantenna placed on top of a gated graphene layer. b) Near-field images of the h-BN nanoantenna on top of graphene with Fermi levels $E_F = 0$ eV (left) and $E_F = 0.25$ eV (right). c) Calculated images for the cases shown in (b). d) Calculated near-field spectra of the square h-BN nanoantenna on top of graphene with Fermi levels $E_F = 0$ eV (black solid line), $E_F = 0.15$ eV (blue solid line), $E_F = 0.25$ eV (red solid line), $E_F = 0.45$ eV (green solid line), and $E_F = 0.6$ eV (cyan solid line). The insets represent the field distribution of the c1 mode at the shifted resonance peaks. The orange dashed vertical line represents the incident frequency $\omega_0 = 1520$ cm^{-1} in (b) and (c). When the resonance peak corresponding to the c1 mode is far from the incident frequency (e.g., $E_F = 0$ and 0.15 eV), the experimental near-field patterns (insets framed by black and blue squares) show a dark area in the center, while it changes to a bright spot (inset framed by red square) for the case that c1-mode resonance peak is close to the incident frequency (e.g., $E_F = 0.25$ eV). Scale bar: 250 nm.

frequency for the c1 mode (whose field distribution can be found in the insets in Figure 4d) shifts from $\omega_{\text{res-c1}} \approx 1511$ cm^{-1} for $E_F = 0$ eV (black line in Figure 4d) to $\omega_{\text{res-c1}} \approx 1518$ cm^{-1} for $E_F = 0.25$ eV (red line in Figure 4d), i.e., for moderately doped graphene. For heavily doped graphene ($E_F = 0.6$ eV, cyan line in Figure 4d), it further shifts toward $\omega_{\text{res-c1}} \approx 1530$ cm^{-1}. As shown in the insets in Figure 4d, the experimental near-field patterns show a dark area in the center of the h-BN nanoantenna for the case of $E_F = 0$ and 0.25 eV. However, it changes to a bright spot when $E_F = 0.25$ eV. Given that the near-field signal in the center is mainly determined by the c1 mode (Figure 2), such change from dark to bright in the experimental near-field images agrees well with the calculated near-field spectra, where the resonance peak corresponding to c1 mode gets closer and closer to the incident frequency ($\omega_0 = 1520$ cm^{-1}) when E_F increases from 0 to 0.25 eV. Note that the linewidths of these actively tuned resonances ($\Delta\omega_{\text{res}} \approx 20$ cm^{-1}) are larger than those in bare h-BN nanoantennas ($\Delta\omega_{\text{res}} \approx 9$ cm^{-1}), which can be explained by the unavoidable introduction of Ohmic losses due to the presence of graphene. However, such linewidths are still more than one order of magnitude smaller than those typically obtained for IR plasmonic nanoantennas made of noble metals ($\Delta\omega_{\text{res}} > 400$ cm^{-1})[25] or graphene ($\Delta\omega_{\text{res}} \approx 200$ cm^{-1}).[18] We notice that such active tunability of PhP resonances in

h-BN nanoantennas can be alternatively seen as a result of the coupling (hybridization) between graphene plasmon polaritons and PhPs (see Figure S6 in the Supporting Information). Such vision goes in line with other recent experimental[38] and theoretical[51] studies. This result implies that our phononic nanoantennas combined with graphene not only relax the restriction of Ohmic losses in graphene plasmonic nanoantennas but also preserve their dynamically tuning capability, thus paving the path for next-generation switchable integrated photonics devices at IR frequencies.

6. Conclusion

We report active and passive tuning of ultranarrow polaritonic resonances in square h-BN nanoantennas. In particular, we demonstrate that these large-Q resonances can be effectively modulated over a wide spectral range by tailoring their dielectric environment passively, which is carried out by either placing them on different substrates, or simply covering them with nanometer-thick layers of WSe$_2$. More importantly, we demonstrate reversible in situ (active) tuning of narrow resonances ($\Delta\omega_{\text{res}} \approx 20$ cm^{-1}) in these nanoantennas when they are placed on top of a graphene layer, which promises applications

**ADVANCED
SCIENCE NEWS**
www.advancedsciencenews.com

**ADVANCED
MATERIALS**
www.advmat.de

based on tunable spectral selectivity or strong light–matter interactions. Furthermore, we find that the polaritonic modes associated with these dynamic resonances provide extraordinary near-field features such as a deep-subwavelength focus ($\approx \lambda_0/42$) of mid-IR light. Altogether, our results introduce tunable phononic nanoantennas as promising building blocks for the development of IR nanodevices, including biosensors and narrowband thermal emitters.

7. Experimental Section

Sample Preparation: The square h-BN nanoantennas were prepared by patterning boron-10 isotopically enriched h-BN flakes.[43] To do this, mechanical exfoliation from bulk h-BN materials was first performed using Nitto tape (Nitto Denko Co., SPV 224P). Afterward, a second exfoliation of the h-BN flakes from the initial tape to a transparent poly(dimethylsiloxane) (PDMS) stamp was performed. Subsequently, they were onto a SiO$_2$/Si substrate using the dry transfer technique.[52] The square-shaped h-BN nanoantennas were defined in the h-BN flakes by high-resolution electron beam lithography.[45] To place the nanoantennas on different substrates, they were picked up using a stamp formed by a PDMS film covered with a layer of polypropylene carbonate (PC),[53] which was mounted in a micromanipulator. After the attached nanoantennas were precisely aligned and contacted on the target substrates, they were up to 200 °C in order to peel off the PDMS from the PC. Finally, to remove the PC layer, the sample was immersed into chloroform solvent at 70 °C. The same h-BN nanoantenna was covered with thin layers of WSe$_2$ (exfoliated using Nitto tape and PDMS stamp) with thicknesses of 31 and 11 nm, respectively.

Nanoimaging Experiments: The nanoimaging experiments were performed using a commercial s-SNOM system (Neaspec GmbH) equipped with a quantum cascade laser (Daylight Solutions), spanning from 1400 to 1600 cm^{-1}. The s-SNOM was based on an atomic force microscopy (AFM) operating in the tapping mode with $\Omega \approx 280$ kHz and an amplitude of $\approx$100 nm. Commercial metal-coated (Pt/Ir) AFM tips (ARROW-NCPt-50, Nanoworld) were employed. The sample was illuminated with a p-polarized mid-IR laser beam from the quantum cascade laser and the p-component of the tip-scattered light was collected with a parabolic mirror. To effectively suppress the background, the detected signals were demodulated at the 3rd harmonic. Pseudoheterodyne interferometry was employed to extract both the amplitude and the phase of the near field.

Numerical Simulations of s-SNOM Images, Near-Field Spectra, and Mode Dispersions: The full-wave numerical simulations shown in Figures 2–4 were performed by using a finite element method (COMSOL). In the simulated model, the AFM tip was approximated by a vertically oriented electric dipole source. It was assumed that the vertical component of the electric field ($|E_z|$) below the dipole mimicked the near-field signal detected in s-SNOM measurements. This simple model had shown an excellent agreement with the experiment for both graphene nanoresonators[46] and h-BN linear antennas.[26]

For reproducing the experimental near-field images, the dipole above the square h-BN nanoantennas was scanned at a fixed imaging frequency ω_0, $|E_z|$ was recorded as a function of the dipole position, and the simulated near-field images (Figures 2b,c and 4c) were obtained. For calculating the near-field spectra (Figures 2a, 3c,f, and 4d), the dipole was located at one fixed position and $|E_z|$ was calculated as a function of ω_0. For analyzing the electric field distribution of individual modes (Figures 2b,c, 3c,f (insets), and 4d), Re(E_z) was calculated in the x–y plane 30 nm above the h-BN nanoantennas at a fixed dipole position and imaging frequency. In all simulations, the height of the dipole above the nanoantennas was fixed to 300 nm. The simulations of the covered nanoantennas considered that the upper WSe$_2$ layer was not in contact with the sidewalls of the nanoantennas. For calculating the dispersions of the M0 and SM0 modes (Figure 1f), the quasinormal mode analysis implemented in COMSOL was employed and both the material anisotropy and losses were considered. From the mode analysis, the complex wavevectors of the PhPs, along with their electromagnetic field distributions, were obtained.

Model for Graphene Conductivity and Electrostatic Tuning of the Chemical Potential: Within the random phase approximation, the graphene conductivity could be expressed as a sum of the intraband and interband contributions[54,55]

$$\sigma = \sigma_{\text{intra}} + \sigma_{\text{inter}} \tag{1}$$

The intraband and interband contributions read

$$\sigma_{\text{intra}} = \frac{2ie^2 t}{\hbar \pi \Omega} \ln\left[2\cosh\left(\frac{1}{2t}\right)\right] \tag{2}$$

$$\sigma_{\text{inter}} = \frac{e^2}{4\hbar}\left[\frac{1}{2} + \frac{1}{\pi}\arctan\left(\frac{\Omega - 2}{2t}\right) - \frac{i}{2\pi}\ln\frac{(\Omega + 2)^2}{(\Omega - 2)^2 + (2t)^2}\right] \tag{3}$$

where $\Omega = \hbar\omega/\mu$, $t = T/\mu$, and μ is the chemical potential, with temperature T expressed in units of energy. A finite relaxation time could be taken into account by substituting ω by $\omega + i\tau^{-1}$ in σ_{intra}.

The chemical potential of graphene depended upon transverse electric field via a DC biased gated structure, thus allowing for an active tuning of the graphene conductivity. The applied DC voltage (V_{DC}) modified the graphene carrier density (n_s) as[56]

$$C_{\text{ox}} V_{\text{DC}} = q_e n_s \tag{4}$$

where $C_{\text{ox}} = \varepsilon_{\text{SiO}_2}\varepsilon_0 / t$ is the gate capacitance, and $\varepsilon_{\text{SiO}_2}$ and t are the permittivity constant and the thickness of the SiO$_2$ that acted as a gate dielectric. This approximation was valid for small dielectric constants (such as that of SiO$_2$, $\varepsilon_{\text{SiO}_2} \approx 2$) and thicknesses larger than several nanometers ($t = 280$ nm in the measured sample). The carrier density was related to the chemical potential μ following the expression

$$n_s = \frac{2}{\pi \hbar^2 v_f^2} \int_{\infty}^{0} \varepsilon\left[f_d(\varepsilon - \mu) - f_d(\varepsilon + \mu)\right] d\varepsilon \tag{5}$$

where ε is the energy, v_f is the Fermi velocity ($\approx 10^6$ m s^{-1}). By solving the previous two equations, an approximated closed-form expression that relates μ and V_{DC} could be obtained

$$\mu \approx \hbar v_f \sqrt{\frac{\pi C_{\text{ox}} V_{\text{DC}}}{q}} \tag{6}$$

This expression was used to relate the capacitance measurements with the chemical potential of graphene.

Supporting Information

Supporting Information is available from the Wiley Online Library or from the author.

Acknowledgements

**ADVANCED
SCIENCE NEWS**

www.advancedsciencenews.com

**ADVANCED
MATERIALS**

www.advmat.de

Conflict of Interest

The authors declare no conflict of interest.

Author Contributions

J.D. and F.J.A.-M. contributed equally to this work. J.D. and P.A.-G. conceived the study. A.Y.N. and P.A.-G. supervised the project. J.D. fabricated the samples and carried out the near-field imaging measurements with the help of J.T.-G., I.D., A.B., A.I.F.T.-M., and J.M.-S. F.J.A.-M. conducted numerical simulations. E.T., D.A.B., and P.J.-H. contributed to the fabrication of gated graphene samples. S.L. and J.H.E. provided the isotopically enriched boron nitride. J.D., F.J.A.-M., R.H., A.Y.N., and P.A.-G. participated in data analysis. J.D., F.J.A.-M., G.A.-P., A.Y.N., and P.A.-G. cowrote the paper with input from the rest of authors.

Data Availability Statement

The data that support the findings of this study are available from the corresponding author upon reasonable request.

Keywords

narrow resonance, optical nanoantenna, phonon polaritons, tunability

[1] V. M. Agranovich, *Surface Polaritons*, Elsevier, Amsterdam, The Netherlands **2012**.

[2] D. N. Basov, M. M. Fogler, F. G. García de Abajo, *Science* **2016**, *354*, aag1992.

[3] T. Low, A. Chaves, J. D. Caldwell, A. Kumar, N. X. Fang, P. Avouris, T. F. Heinz, F. Guinea, L. Martin-Moreno, F. Koppens, *Nat. Mater.* **2017**, *16*, 182.

[4] I. Epstein, D. Alcaraz, Z. Huang, V.-V. Pusapati, J.-P. Hugonin, A. Kumar, X. M. Deputy, T. Khodkov, T. G. Rappoport, J.-Y. Hong, *Science* **2020**, *368*, 1219.

[5] H. Xu, E. J. Bjerneld, M. Käll, L. Börjesson, *Phys. Rev. Lett.* **1999**, *83*, 4357.

[6] R. Zhang, Y. Zhang, Z. C. Dong, S. Jiang, C. Zhang, L. G. Chen, L. Zhang, Y. Liao, J. Aizpurua, Y. Luo, J. L. Yang, J. G. Hou, *Nature* **2013**, *498*, 82.

[7] J. N. Anker, W. P. Hall, O. Lyandres, N. C. Shah, J. Zhao, R. P. Van Duyne, *Nat. Mater.* **2008**, *7*, 442.

[8] F. Koppens, T. Mueller, P. Avouris, A. Ferrari, M. Vitiello, M. Polini, *Nat. Nanotechnol.* **2014**, *9*, 780.

[9] M. Schnell, P. Alonso-Gonzalez, L. Arzubiaga, F. Casanova, L. E. Hueso, A. Chuvilin, R. Hillenbrand, *Nat. Photonics* **2011**, *5*, 283.

[10] M. Schnell, A. García-Etxarri, A. Huber, K. Crozier, J. Aizpurua, R. Hillenbrand, *Nat. Photonics* **2009**, *3*, 287.

[11] P. Roelli, C. Galland, N. Piro, T. J. Kippenberg, *Nat. Nanotechnol.* **2016**, *11*, 164.

[12] H. Hu, X. Yang, X. Guo, K. Khaliji, S. R. Biswas, F. J. García de Abajo, T. Low, Z. Sun, Q. Dai, *Nat. Commun.* **2019**, *10*, 1131.

[13] H. Hu, X. Yang, F. Zhai, D. Hu, R. Liu, K. Liu, Z. Sun, Q. Dai, *Nat. Commun.* **2016**, *7*, 12334.

[14] J. B. Khurgin, *Nat. Nanotechnol.* **2015**, *10*, 2.

[15] G. X. Ni, A. S. McLeod, Z. Sun, L. Wang, L. Xiong, K. W. Post, S. S. Sunku, B.-Y. Jiang, J. Hone, C. R. Dean, M. M. Fogler, D. N. Basov, *Nature* **2018**, *557*, 530.

[16] J. Chen, M. Badioli, P. Alonso-González, S. Thongrattanasiri, F. Huth, J. Osmond, M. Spasenović, A. Centeno, A. Pesquera, P. Godignon, *Nature* **2012**, *487*, 77.

[17] Z. Fei, A. Rodin, G. O. Andreev, W. Bao, A. McLeod, M. Wagner, L. Zhang, Z. Zhao, M. Thiemens, G. Dominguez, *Nature* **2012**, *487*, 82.

[18] D. Rodrigo, O. Limaj, D. Janner, D. Etezadi, F. J. García de Abajo, V. Pruneri, H. Altug, *Science* **2015**, *349*, 165.

[19] L. Ju, B. Geng, J. Horng, C. Girit, M. Martin, Z. Hao, H. A. Bechtel, X. Liang, A. Zettl, Y. R. Shen, *Nat. Nanotechnol.* **2011**, *6*, 630.

[20] H. Hu, F. Zhai, D. Hu, Z. Li, B. Bai, X. Yang, Q. Dai, *Nanoscale* **2015**, *7*, 19493.

[21] J. Duan, S. Xiao, J. Chen, *Adv. Sci.* **2019**, *6*, 1801974.

[22] F. H. Koppens, D. E. Chang, F. J. García de Abajo, *Nano Lett.* **2011**, *11*, 3370.

[23] A. Woessner, M. B. Lundeberg, Y. Gao, A. Principi, P. Alonso-González, M. Carrega, K. Watanabe, T. Taniguchi, G. Vignale, M. Polini, J. Hone, R. Hillenbrand, F. H. L. Koppens, *Nat. Mater.* **2015**, *14*, 421.

[24] J. D. Caldwell, L. Lindsay, V. Giannini, I. Vurgaftman, T. L. Reinecke, S. A. Maier, O. J. Glembocki, *Nanophotonics* **2015**, *4*, 44.

[25] M. Autore, P. Li, I. Dolado, F. J. Alfaro-Mozaz, R. Esteban, A. Atxabal, F. Casanova, L. E. Hueso, P. Alonso-González, J. Aizpurua, *Light: Sci. Appl.* **2018**, *7*, 17172.

[26] F. Alfaro-Mozaz, P. Alonso-González, S. Vélez, I. Dolado, M. Autore, S. Mastel, F. Casanova, L. Hueso, P. Li, A. Y. Nikitin, *Nat. Commun.* **2017**, *8*, 15624.

[27] M. Tamagnone, K. Chaudhary, A. Zhu, M. Meretska, J. Li, J. H. Edgar, A. Ambrosio, F. Capasso, arXiv: 1905.02177, **2019**.

[28] M. Autore, I. Dolado, P. Li, R. Esteban, F. J. Alfaro-Mozaz, A. Atxabal, S. Liu, J. H. Edgar, S. Vélez, F. Casanova, *Adv. Opt. Mater.* **2021**, *9*, 2001958.

[29] W. Ma, P. Alonso-González, S. Li, A. Y. Nikitin, J. Yuan, J. Martín-Sánchez, J. Taboada-Gutiérrez, I. Amenabar, P. Li, S. Vélez, *Nature* **2018**, *562*, 557.

[30] Z. Zheng, N. Xu, S. L. Oscurato, M. Tamagnone, F. Sun, Y. Jiang, Y. Ke, J. Chen, W. Huang, W. L. Wilson, *Sci. Adv.* **2019**, *5*, eaav8690.

[31] J. Taboada-Gutiérrez, G. Álvarez-Pérez, J. Duan, W. Ma, K. Crowley, I. Prieto, A. Bylinkin, M. Autore, H. Volkova, K. Kimura, *Nat. Mater.* **2020**, *19*, 964.

[32] J. D. Caldwell, I. Aharonovich, G. Cassabois, J. H. Edgar, B. Gil, D. Basov, *Nat. Rev. Mater.* **2019**, *4*, 552.

[33] S. Dai, Q. Ma, T. Andersen, A. S. Mcleod, Z. Fei, M. K. Liu, M. Wagner, K. Watanabe, T. Taniguchi, M. Thiemens, F. Keilmann, P. Jarillo-Herrero, M. M. Fogler, D. N. Basov, *Nat. Commun.* **2015**, *6*, 6963.

[34] P. Li, M. Lewin, A. V. Kretinin, J. D. Caldwell, K. S. Novoselov, T. Taniguchi, K. Watanabe, F. Gaussmann, T. Taubner, *Nat. Commun.* **2015**, *6*, 7507.

[35] J. D. Caldwell, A. V. Kretinin, Y. Chen, V. Giannini, M. M. Fogler, Y. Francescato, C. T. Ellis, J. G. Tischler, C. R. Woods, A. J. Giles, *Nat. Commun.* **2014**, *5*, 5221.

[36] F. Neubrech, C. Huck, K. Weber, A. Pucci, H. Giessen, *Chem. Rev.* **2017**, *117*, 5110.

[37] F. Neubrech, A. Pucci, T. W. Cornelius, S. Karim, A. García-Etxarri, J. Aizpurua, *Phys. Rev. Lett.* **2008**, *101*, 157403.

[38] S. Dai, Q. Ma, M. Liu, T. Andersen, Z. Fei, M. Goldflam, M. Wagner, K. Watanabe, T. Taniguchi, M. Thiemens, *Nat. Nanotechnol.* **2015**, *10*, 682.

[39] X. Yang, F. Zhai, H. Hu, D. Hu, R. Liu, S. Zhang, M. Sun, Z. Sun, J. Chen, Q. Dai, *Adv. Mater.* **2016**, *28*, 2931.

[40] S. Dai, Z. Fei, Q. Ma, A. Rodin, M. Wagner, A. McLeod, M. Liu, W. Gannett, W. Regan, K. Watanabe, *Science* **2014**, *343*, 1125.

[41] J. Duan, R. Chen, J. Li, K. Jin, Z. Sun, J. Chen, *Adv. Mater.* **2017**, *29*, 1702494.

[42] P. Li, I. Dolado, F. Alfaro-Mozaz, A. Y. Nikitin, F. Casanova, L. Hueso, S. Vélez, R. Hcillenbrand, *Nano Lett.* **2017**, *17*, 228.

[43] A. J. Giles, S. Dai, I. Vurgaftman, T. Hoffman, S. Liu, L. Lindsay, C. T. Ellis, N. Assefa, I. Chatzakis, T. L. Reinecke, *Nat. Mater.* **2018**, *17*, 134.

[44] S. Dai, M. Tymchenko, Y. Yang, Q. Ma, M. Pita-Vidal, K. Watanabe, T. Taniguchi, P. Jarillo-Herrero, M. M. Fogler, A. Alù, D. N. Basov, *Adv. Mater.* **2018**, *30*, 1706358.

[45] I. Dolado, F. J. Alfaro-Mozaz, P. Li, E. Nikulina, A. Bylinkin, S. Liu, J. H. Edgar, F. Casanova, L. E. Hueso, P. Alonso-González, *Adv. Mater.* **2020**, *32*, 1906530.

[46] A. Nikitin, P. Alonso-González, S. Vélez, S. Mastel, A. Centeno, A. Pesquera, A. Zurutuza, F. Casanova, L. Hueso, F. Koppens, *Nat. Photonics* **2016**, *10*, 239.

[47] A. Fali, S. T. White, T. G. Folland, M. He, N. A. Aghamiri, S. Liu, J. H. Edgar, J. D. Caldwell, R. F. Haglund, Y. Abate, *Nano Lett.* **2019**, *19*, 7725.

[48] A. M. Dubrovkin, B. Qiang, T. Salim, D. Nam, N. I. Zheludev, Q. J. Wang, *Nat. Commun.* **2020**, *11*, 1863.

[49] J. B. Khurgin, G. Sun, *Appl. Phys. Lett.* **2011**, *99*, 211106.

[50] F. L. Ruta, A. J. Sternbach, A. B. Dieng, A. S. McLeod, D. N. Basov, *Nano Lett.* **2020**, *20*, 7933.

[51] A. Kumar, T. Low, K. H. Fung, P. Avouris, N. X. Fang, *Nano Lett.* **2015**, *15*, 3172.

[52] A. Castellanos-Gomez, M. Buscema, R. Molenaar, V. Singh, L. Janssen, H. S. van der Zant, G. A. Steele, *2D Mater.* **2014**, *1*, 011002.

[53] R. Frisenda, E. Navarro-Moratalla, P. Gant, D. P. De Lara, P. Jarillo-Herrero, R. V. Gorbachev, A. Castellanos-Gomez, *Chem. Soc. Rev.* **2018**, *47*, 53.

[54] A. Y. Nikitin, F. Guinea, F. Garcia-Vidal, L. Martin-Moreno, *Phys. Rev. B* **2011**, *84*, 195446.

[55] B. Wunsch, T. Stauber, F. Sols, F. Guinea, *New J. Phys.* **2006**, *8*, 318.

[56] J.-S. Gómez-Díaz, J. Perruisseau-Carrier, *Opt. Express* **2013**, *21*, 15490.